Petroleum Science 20 (2023) 803–814

Contents lists available at ScienceDirect

Petroleum Science

journal homepage: www.keaipublishing.com/en/journals/petroleum-science

Original Paper

Laboratory insights into the effects of methane hydrate on the anisotropic joint elastic-electrical properties in fractured sandstones

Sheng-Biao Liu [a], Tong-Cheng Han [a, b, *], Li-Yun Fu [a, b]

[a] Shandong Provincial Key Laboratory of Deep Oil and Gas, China University of Petroleum (East China), Qingdao, Shandong, 266580, China
[b] Laboratory for Marine Mineral Resources, Pilot National Laboratory for Marine Science and Technology, Qingdao, Shandong, 266071, China

ARTICLE INFO

Article history:
Received 10 February 2022
Received in revised form
27 June 2022
Accepted 14 September 2022
Available online 19 September 2022

Edited by Jie Hao

Keywords:
Fractured hydrate reservoirs
Elastic anisotropy
Electrical anisotropy
Joint elastic-electrical properties
Hydrate distribution

ABSTRACT

Fractured hydrate-bearing reservoirs show significantly anisotropic geophysical properties. The joint application of seismic and electromagnetic explorations is expected to accurately assess hydrate resources in the fractured reservoirs. However, the anisotropic joint elastic-electrical properties in such reservoirs that are the key to the successful application of the joint explorations, remain poorly understood. To obtain such knowledge, we designed and implemented dedicated laboratory experiments to study the anisotropic joint elastic-electrical properties in fractured artificial silica sandstones (with fracture density of about 6.2%, porosity of approximately 25.7%, and mean grainsize of 0.089 mm) with evolving methane hydrate. The experimental results showed that the anisotropic compressional wave velocities respectively increased and decreased with the forming and dissociating hydrate, and the variation in the increasing trend and the decreasing extent of the velocity perpendicular to the fractures were more significant than that parallel to the fractures, respectively. The experimental results also showed that the overall decreasing trend of the electrical conductivity parallel to the fractures was steeper than that perpendicular to the fractures during hydrate formation, and the general variations of the two conductivities with complex trend were similar during hydrate dissociation. The variations in the elastic and electrical anisotropic parameters with forming and dissociating hydrate were also found to be distinct. Interpretation of the experimental results suggested that the hydrate binding to the grains evolved to bridge the surfaces of fractures when saturation exceeded 10% during hydrate formation, and the bridging hydrate gradually evolved to floating in fractures during dissociation. The experimental results further showed that the anisotropic velocities and electrical conductivities were correlated with approximately consistent trends of different slopes during hydrate formation, and the joint elastic-electrical anisotropic parameters exhibited a sharp peak at the hydrate saturation of about 10%. The results suggested that the anisotropic joint properties can be employed not only to accurately estimate hydrate saturation but also possibly to identify hydrate distribution in the fractures.

1. Introduction

Natural gas hydrate is ice-like solid substance composed of natural gas (mostly methane) and water at the conditions of low temperature and high pressure (Sloan and Koh, 2007), and is widely distributed in marine sediments and permafrost regions (Kvenvolden, 1993). As a type of clean energy, natural gas hydrate has attracted increasing attention due to its vast energy resource (Boswell and Collett, 2011) and the potential natural disasters (e.g., submarine landslide, global warming) caused by its dissociation (Archer et al., 2009; Sultan et al., 2004). Seismic and electromagnetic explorations are among the most important geophysical survey applications for the quantitative assessment of hydrate resources (Attias et al., 2016; Goswami et al., 2015; Miyakawa et al., 2014). The elastic and electrical properties that are respectively detected by the seismic and electromagnetic methods are independent and complementary. Therefore, the joint application of seismic and electromagnetic explorations is expected to provide a more accurate assessment of hydrate resources (Attias et al., 2020; Goswami et al., 2015; Han et al., 2011; Han, 2018; Liu et al., 2020).

* Corresponding author. Shandong Provincial Key Laboratory of Deep Oil and Gas, China University of Petroleum (East China), Qingdao, Shandong, 266580, China.
E-mail address: hantc@upc.edu.cn (T.-C. Han).

https://doi.org/10.1016/j.petsci.2022.09.007

However, the key to the successful interpretation of joint seismic and electromagnetic survey data relies on the establishment of a reliable relationship between the elastic and electrical properties (i.e., the joint elastic-electrical properties) in hydrate-bearing reservoirs.

Various well-designed laboratory experiments have been carried out to obtain the knowledge of the elastic and electrical properties in hydrate-bearing reservoirs (Bu et al., 2019; Hu et al., 2010, 2012; Li et al., 2020; Ren et al., 2010; Sahoo et al., 2018a). While the experimental studies have demonstrated a simultaneous enhancement in the elastic velocity and reduction in the electrical conductivity of the background media with gas hydrate (Ren et al., 2010; Sahoo et al., 2018a), they do not give explicitly how the elastic and electrical properties are correlated as gas hydrate evolves. Complementarily, theoretical modeling has been performed to investigate more directly the relationships between the elastic and electrical properties in hydrate-bearing reservoirs (Attias et al., 2020; Goswami et al., 2015; Liu et al., 2020; Sava et al., 2008). Combined with the experimental understanding, theoretical studies reveal a general negative correlation between the elastic velocity and electrical conductivity as hydrate saturation increases (Attias et al., 2020; Liu et al., 2020; Sava et al., 2008), and illustrate that the specific variations of the negative correlations are dependent on the distribution (e.g., pore-floating, bridging, and cementing) of gas hydrate in the pore space that has a significantly different impact on the elastic and electrical properties, respectively (Jin et al., 2020; Spangenberg and Kulenkampff, 2006; Sahoo et al., 2018a; Schindler et al., 2017; Priest et al., 2009). The modeled joint elastic-electrical correlations have been successfully applied to the joint interpretation of seismic and electromagnetic exploration data in hydrate-bearing reservoirs to improve the quantitative assessment of hydrate resources (Attias et al., 2020; Goswami et al., 2015).

However, the joint elastic-electrical properties obtained above are based on isotropic hydrate-bearing reservoirs, and thus their application to anisotropic reservoirs may be problematic because the influences of gas hydrate on the physical properties of anisotropic media can be distinct in different directions (Cook, 2010; Kumar et al., 2006; Lee, 2009; Lee and Collett, 2009; Liu et al., 2021a, 2021b; Peng et al., 2019; Singhroha et al., 2020), and hence the joint correlations may also vary with the measurement directions. Fractured hydrate-bearing reservoirs that have been extensively discovered across the world (Dai et al., 2012; Daigle and Dugan, 2010; Peng et al., 2019; Singhroha et al., 2020; You et al., 2019), are typical anisotropic reservoirs caused predominantly by the aligned fractures due to stress orientation or tectonic movement (Wang and Tang, 2005; Xu et al., 2018; You et al., 2019). Several publications using the methods of theoretical modeling and laboratory experiments have studied the anisotropic elastic and electrical properties independently (Ghosh et al., 2010; Lee, 2009; Lee and Collett, 2009; Liu et al., 2021a, 2021b), and have illustrated that the evolution of hydrate distribution in the fractures plays an important role on the anisotropic elastic and electrical behaviors. However, the explicit correlations between the elastic and electrical properties in the different directions of fractured hydrate-bearing reservoirs remain elusive.

This work aims to investigate, through dedicated laboratory experiments, the anisotropic joint elastic-electrical properties in fractured artificial sandstones with evolving hydrate. We first manufacture the required sandstone samples with aligned penny-shaped fractures parallel to the layers and measure the anisotropic compressional wave velocities and electrical conductivities of the synthetic samples during hydrate formation and dissociation. The differences in the variations of the obtained anisotropic compressional wave velocities, anisotropic electrical conductivities, and anisotropic joint elastic-electrical properties with hydrate saturation are then presented and studied. Finally, the experimental results are analyzed and interpreted in terms of the evolution of hydrate distribution in the fractures.

2. Laboratory experiments

2.1. Synthetic sandstone samples with aligned fractures

A sandstone block with aligned penny-shape fractures was synthesized for the experiments, using the method similar to that described by Ding et al. (2017). We mixed thoroughly different sized sand, feldspar and kaolinite with aqueous sodium silicate gel, and packed a predetermined volume of the above mixture into a sample mould in successive layers. The different sized sand determined the mean grainsize of 0.089 mm of the sandstone block. We evenly laid a certain number of special paper discs (made by Nitrate cellulose material) with diameter of 3 mm and thickness of 0.065 mm (giving rise to fracture aspect ratio of about 0.022) on each layer of the mixture for the formation of the penny-shaped fractures. The fracture density of the block was calculated to be about 6.2% based on the number and radius of paper discs as well as the volume of the block (Mavko et al., 2009). The mixture in the mould was compacted under the mechanical pressure of 100 MPa for 24 h to obtain a consolidated block, which was then put into a baking oven and heated at the temperature of 60 °C for 48 h for further consolidation. Finally, the consolidated block was placed into a muffle oven and sintered at the temperature of 1200 °C for 8 h to make the sodium silicate and kaolinite transform to silica, and to decompose the paper discs to leave penny-shaped voids (fractures) with the orientation parallel to the layering. The pore structure of the obtained sandstone that was visualized by the scanning electronic microscopy, presented the features of the normal pores and the fractures, as shown in Fig. 1.

The obtained sandstone block with aligned fractures can be regarded as a transversely isotropic (TI) medium. We cored two cylindrical plugs from the block at 0° and 90° relative to the normal of the aligned fractures, denoted as sample F-0 and F-90,

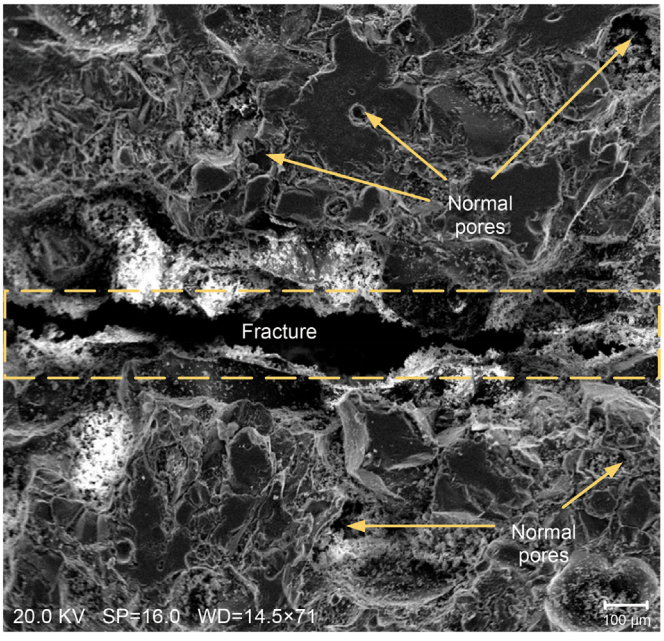

Fig. 1. SEM image of the artificial sandstone with aligned fractures.

respectively (see Fig. 2). The two cylindrical plugs were about 2.54 cm in diameter with lengths of 4.65 cm and 5.35 cm, respectively. The permeabilities of sample F-0 and F-90 respectively were 1040 mD and 1412 mD measured by the CMS-300 Core Measurement System. The porosities of F-0 and F-90 were measured to be 25.66% and 25.73%, respectively, using a helium porosimeter. Bulk densities of the samples were respectively about 1.838 g/cm^3 and 1.837 g/cm^3 calculated according to the measured volume and weight of the dry samples. The approximately identical porosity and density of the two samples suggested that the difference between the samples can be regarded to be caused solely by the coring direction relative to the layering and the aligned fractures.

2.2. Anisotropic elastic and electrical measurements during hydrate formation and dissociation

The two cylindrical samples were first dried in a baking oven at the temperature of 60 °C for 48 h, and were then separately loaded into a joint elastic-electrical rig (with the configuration shown schematically in Fig. 3), where a constant confining pressure of 20 MPa was applied to seal the sample. Each sample was vacuumed to the pressure of −0.1 MPa for 12 h to remove air from its pore system as well as from the pump-lines of the experimental system. A certain volume of brine made from de-aired and de-stilled water and 35 g/L NaCl and 0.1 g/L dodecyl sulfate (catalyzer of hydrate formation) was then injected into the samples to achieve the predetermined brine saturation of 70%, using an injection pump that accurately measured the brine volume injected into the samples. Subsequently, a pore pressure of 8.05 MPa was pressurized by injecting methane gas through the methane gas steel cylinder. The volume of the methane gas injected into the samples was accurately recorded using a gas volume flow meter. The experimental system was kept static for 24 h to make brine and methane gas distribute uniformly in the pore system (including the normal pores and fractures) of the samples.

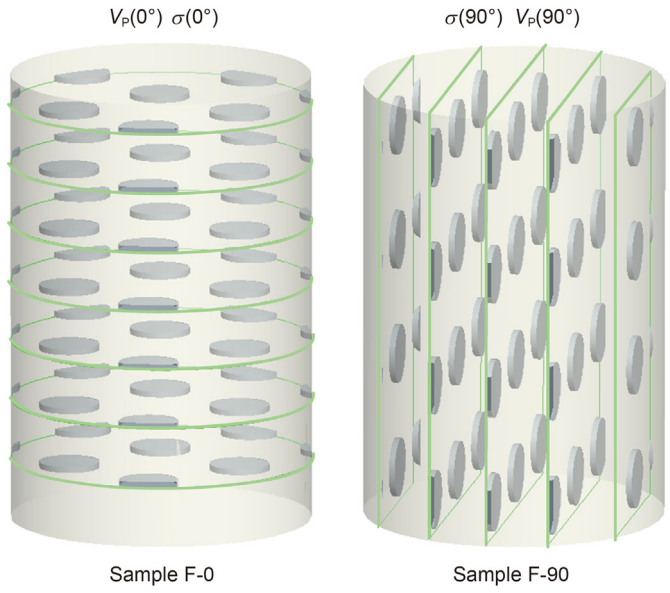

Fig. 2. Schematic diagram showing the cored cylindrical samples with aligned fracturs, and the compressional wave velocities ($V_P(0°)$ and $V_P(90°)$) and electrical conductivities ($\sigma(0°)$ and $\sigma(90°)$) measured in the experiments. Note that $V_P(0°)$ and $\sigma(0°)$ respectively represent the velocity and conductivity at the direction parallel to the fracture normal (i.e., the direction across the fractures), and $V_P(90°)$ and $\sigma(90°)$ respectively indicate the velocity and conductivity at the perpendicular direction relative to the normal of fracture (i.e., the direction along the fractures). The green line frames represent the bedding planes, and the grey discs parallel to the layering indicate the penny-shaped fractures.

Subsequently, a low temperature thermostat (see Fig. 3) that was set to the temperature of 2 °C, was used to cool the experimental system from room temperature (approximately 24 °C) to achieve the hydrate formation conditions. With the decreasing temperature, the pore pressure of the experimental system slowly reduced due to the contraction of methane gas. When the temperature of the experimental system reduced to about 3 °C, the pore pressure started to decrease quickly, indicating the beginning of hydrate formation (Sahoo et al., 2018b). During hydrate formation, the temperature of the experimental system gradually stabilized at 2.5 °C and the pore pressure continuously decreased as a result of the consumption of methane gas until it slowly reached about 4 MPa. We then left the experimental system for several hours to ensure that the pore pressure did not reduce any more, indicating the completion of hydrate formation. In the process of hydrate formation, the compressional waveform was measured at an interval of approximately 10 min, and the electrical resistance was recorded every 0.2 s by the experimental system unless the elastic measurements were performed. After hydrate formation finished, the thermostat was turned off to allow the temperature of experimental system to increase to dissociate the hydrate, during which process, the pore pressure continuously increased due to the hydrate dissociation and the expansion of methane gas with increasing temperature. The pore pressure and temperature of the experimental system gradually stabilized at 8.05 MPa and 24 °C, respectively, implying the complement of hydrate dissociation. During hydrate dissociation, the elastic measurements were performed at an interval of about 15 min, and the electrical measurements were monitored every 0.2 s and would be temporarily halted for the elastic measurements. Throughout the experiments, the pore pressure and the temperature were respectively monitored by a pressure sensor with accuracy of ±0.2% and a temperature sensor with accuracy of ±0.1% to calculate the varying hydrate saturation, using the P-T method described by (Sahoo et al., 2018b). The error of hydrate saturation calculation was estimated to be about ±0.3%, more details of the error estimation were provided by Liu et al. (2021b).

After the joint elastic and electrical measurements during hydrate formation and dissociation, the anisotropic samples were taken out from the joint elastic-electrical rig, and were washed and dried. The dry samples were separately loaded into the joint elastic-electrical rig again, and then vacuumed and saturated at 70% using the same brine as in the hydrate experiments. We then injected nitrogen gas into the samples to provide varying pore pressure (from 3.5 MPa to 8 MPa at an interval of 0.5 MPa) consistent with that in the hydrate experiments. The anisotropic electrical measurements were repeated at each nitrogen pore pressure at the temperature of 3 °C to distinguish the effects of changing pore pressure from the forming hydrate on the electrical conductivities of the samples. In addition, to understand the effects of the varying temperature on the electrical properties, the anisotropic electrical measurements were first carried out in the temperature range from 25 °C to 5 °C at an interval of 2 °C, and were then performed every 0.4 °C until the temperature reached 2.5 °C. When the electrical properties were measured with the varying temperatures, the pore pressure was kept at 8 MPa provided by nitrogen gas. The above calibration experiments were to understand the different effects of hydrate and the varying pore pressure and temperature on the electrical properties.

The measurement frequencies of the ultrasonic and electrical system were 0.5 MHz and 1 kHz, respectively. The arrival time of the first trough of the measured compressional waveform was read as the total wave traveling time in the sample and in the transducers, because the arrival time of the first trough could be more

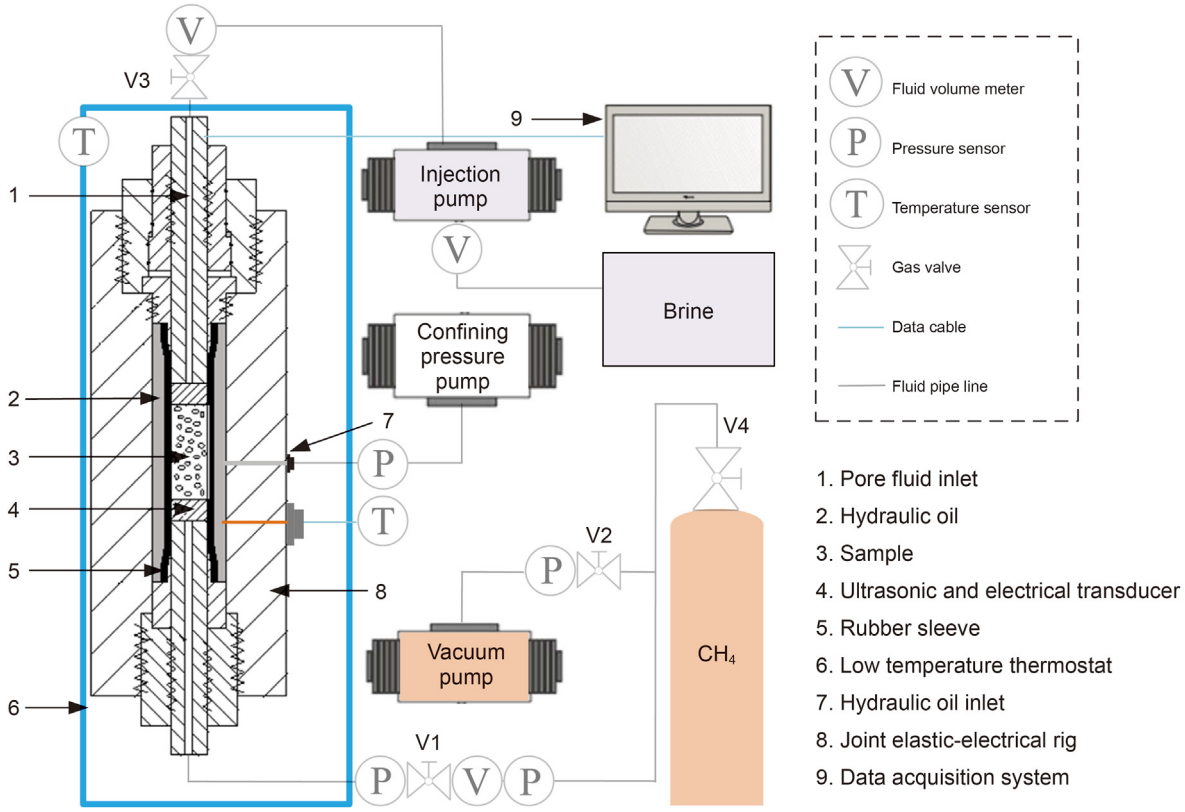

Fig. 3. Schematic representation of the experimental setup. The joint elastic-electrical rig continuously records the electrical resistance and measures the waveform of compressional wave. The electrical resistance and the compressional waveform are measured by a two-electrode system and the narrow-band ultrasonic transducers, respectively. Using the two-electrode system, the electrode polarization effect is assumed to be negligible for the samples with high-porosity and high brine salinity (e.g., the samples in this study). As the measurements of compressional waveform are conducted, the record of electrical resistance will be interrupted to avoid interference.

accurately picked up than that of the first break. Three aluminum samples (with lengths of about 3, 4, and 5 cm, respectively) were employed to determine the transmitting time in the transducers, which was calculated via extrapolating the first trough time of the three aluminum samples to the length of 0. The arrival time of the first trough in combination with the length of the samples measured by a vernier caliper with an accuracy of ±0.01 mm was used to calculate the velocity. The electrical resistance was employed to calculate the electrical conductivity of the samples in combination with their length and cross-sectional area. The measurement errors were estimated to be about ±0.8% for compressional wave velocity and approximately ±0.2% for electrical conductivity (Han et al., 2020).

2.3. Calculation of elastic and electrical anisotropic parameters

The calculation of the anisotropic parameters requires the anisotropic properties measured at the same hydrate saturation (i.e., the same sample density). However, since the anisotropic physical properties were collected from two independent experiments, it can be difficult to make sure that the physical properties were measured at the same hydrate saturation. Therefore, we interpolated the velocity data of sample F-0 to obtain its velocity at the same hydrate saturations as that measured from sample F-90, which showed a slower process of hydrate formation and hence the measured data points were denser. We also picked up the anisotropic conductivities at the hydrate saturation where the anisotropic velocities were measured, and then employed the interpolation method to obtain the conductivity of sample F-0 at the same hydrate saturations as that selected conductivity of sample F-90, so that the anisotropic parameters of the elastic and electrical properties can be jointly shown.

The obtained anisotropic velocities and electrical conductivities were used to determine the compressional wave anisotropic parameter (ε) and the electrical anisotropic parameter (λ) of the samples during hydrate formation and dissociation, using theories of Thomsen (1986) and Nabawy et al. (2010), respectively

$$C_{11} = \rho V_P^2(90^\circ), \tag{1}$$

$$C_{33} = \rho V_P^2(0^\circ), \tag{2}$$

$$\varepsilon = \frac{C_{11} - C_{33}}{2C_{33}}, \tag{3}$$

$$\text{and } \lambda = \sqrt{\frac{\sigma(90^\circ)}{\sigma(0^\circ)}}, \tag{4}$$

where C_{11} and C_{33} were the elastic constants for TI media (Mavko et al., 2009), $V_P(0^\circ)$ and $V_P(90^\circ)$ respectively were the compression wave velocities at the directions perpendicular and parallel to the anisotropy plane, $\sigma(0^\circ)$ and $\sigma(90^\circ)$ represent the electrical conductivities across and along the anisotropy plane, respectively, and ρ was the density of each sample, which was determined by the density and porosity of the dry samples as well as the saturation of the brine and hydrate in the samples during hydrate formation and dissociation.

3. Experimental results

Two rounds of experiments for measuring the anisotropic compression wave velocities and electrical conductivities in the artificial sandstones with aligned fractures during hydrate formation and dissociation are performed. The obtained results between the two rounds of experiments show good repeatability. To clearly exhibit the experimental results, only one group of experimental results is shown to analyze and interpret in the following sections.

3.1. Effects of hydrate evolution on the anisotropic elastic properties

Fig. 4 shows the variations of the measured anisotropic compressional wave velocities of the fractured samples with hydrate saturation (S_h) during hydrate formation and dissociation. As a whole, both the velocities increase with hydrate formation and decrease with hydrate dissociation. This can be explained in terms of the variations in the elastic moduli of the samples with hydrate saturation in the pore system (including the normal pores and the fractures). Because the elastic moduli of hydrate are higher than that of methane gas and brine in the pore system, the elastic moduli of the samples can be respectively strengthened and weakened with increasing and decreasing hydrate saturation, and hence the velocities. Fig. 4 also shows that at hydrate saturation of 0% the velocity of sample F-90 (i.e., $V_P(90°)$) is significantly higher than that of the sample F-0 (i.e., $V_P(0°)$). This is the intrinsic anisotropy of the samples caused by the aligned fractures and can be explained by the differences in the anisotropic compressibility of the fractures. The rocks are more difficult to compress in the direction parallel to the fractures than in the direction perpendicular to the fractures, leading to the higher elastic moduli at the direction along the fractures and hence the higher velocity, i.e., $V_P(90°)$.

Apart from the general increase in the velocities during hydrate formation, Fig. 4 also illustrates the significant difference in the increasing rates between the anisotropic velocities during hydrate formation. For hydrate saturation below about 10%, $V_P(0°)$ gently increases with hydrate saturation, and its increasing trend becomes significantly steeper as hydrate saturation further increases ($10\% < S_h < 16\%$). When hydrate saturation is higher than about 16%, the increasing rate of $V_P(0°)$ tends to be moderate. Unlike the significant variation of $V_P(0°)$, the degree of the variation of $V_P(90°)$ during hydrate formation is less notable. While there is significant difference in the variations between the anisotropic velocities during hydrate formation, the two velocities both show relatively smooth decrease with dissociating hydrate, although the extent of the reduction is more dramatic in $V_P(0°)$.

The above observed variations of the anisotropic velocities with forming and dissociating hydrate are similar to the experimental results reported by Liu et al. (2021a), and can be interpreted in terms of the evolution of the hydrate distribution in the aligned fractures. For the initial stage of hydrate formation ($S_h < 10\%$), the forming hydrate may bind to the grains around the surfaces of the fractures, as the reported knowledge based on isotropic media by Yang et al. (2016), i.e., hydrate forms around the quartz grains. Such hydrate distribution can gently enhance the elastic moduli of the fractures. With the further increase of hydrate saturation ($10\% < S_h < 16\%$), the newly forming hydrate can connect the binding hydrate, i.e., the nearby surfaces of the fractures are bridged. Such bridging hydrate distribution can significantly strengthen the elastic moduli in the direction perpendicular to the fractures, but its contribution to the elastic moduli parallel to the fractures can be still less significant. This is simply because there is evidence showing that the existence of aligned fractures does not affect much the moduli of the rock along the fractures (Han et al., 2021b). The formation of bridging hydrate in the fractures with increasing hydrate saturation is similar to the understanding obtained from isotropic media (Liu et al., 2021; Zhao et al., 2015), which indicates that with the increasing amount of hydrate in the pores, hydrate would mechanically support the adjacent grains and hence dramatically enhances the stiffness of the background media. At the final stage of hydrate formation ($S_h > 16\%$), the forming hydrate may continuously bridge the fractures. Nevertheless, the effects of the new bridging hydrate on the enhancement of the elastic moduli perpendicular to the fractures are smaller than before.

During hydrate dissociation, the relatively smooth variation in the velocities and the more significant reduction in $V_P(0°)$ can also be interpreted in terms of the evolution of hydrate distribution in the fractures. To decompose hydrate, the temperature of the

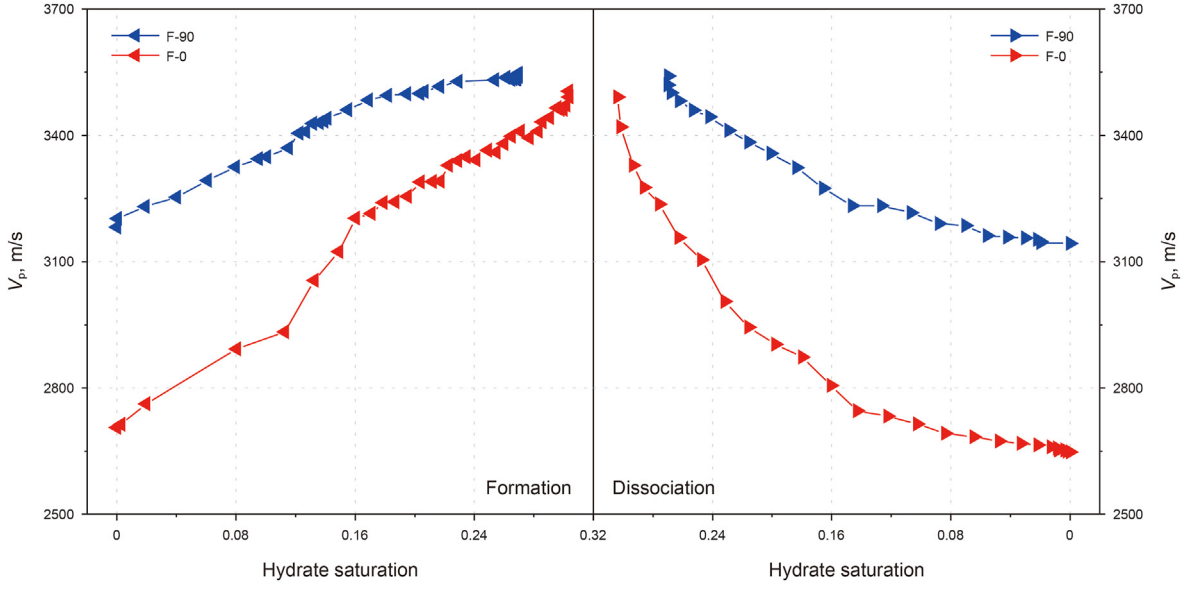

Fig. 4. Variations of the measured anisotropic compressional wave velocities as functions of hydrate saturation during hydrate formation and dissociation. The denser data points during hydrate formation are caused by the fact that the time interval of the elastic measurements during hydrate formation is less than that during hydrate dissociation.

samples is elevated. Therefore, the binding hydrate (the hydrate binding to the grains) dissociates first due to the greater thermal conductivity of the sand grains (Cortes et al., 2009), so that the hydrate with bridging distribution transforms to the floating hydrate. Because of the slow increasing-temperature process of the experimental system, the temperature gradually increases from outside to inside in the samples. As a result, the bridging hydrate evolves to floating hydrate from outside to inside in the samples by degrees, leading to the bulk average of the evolving hydrate distribution in the entire sample. This slow evolution of hydrate distribution during hydrate dissociation gives rise to the gradual decrease in the elastic moduli of the samples. Because fractures affect more significantly the velocity across the fractures, $V_P(0^\circ)$ shows a more dramatic reduction with the dissociating hydrate in the factures.

We have characterized the anisotropic elastic properties of the samples during hydrate formation and dissociation using the measured anisotropic compressional wave velocities. We can also employ the compressional wave anisotropic parameter (Thomsen, 1986) to more directly describe the anisotropic elastic behaviors of the samples. Fig. 5 shows the calculated parameter ε as a function of forming and dissociating hydrate. It can be seen that ε gently decreases at the beginning stage of hydrate formation ($S_h < 10\%$), with the reduction being steeper with the further forming hydrate ($10\% < S_h < 16\%$), and finally becoming moderate for hydrate saturation above 16%. At the hydrate saturation below about 10%, the gentle reduction in ε implies that the enhancement in the elastic moduli perpendicular to the fractures is slightly higher than that at the parallel direction. This again can be explained by the binding hydrate to the grains at the surfaces of the fractures. For hydrate saturation between 10% and 16%, the dramatic decrease of ε indicates that the increase in the elastic moduli across the fractures is more significant than that along the fractures. This further supports our explanation that hydrate bridges the nearby surfaces of the fractures. When hydrate saturation exceeds about 16%, the moderate decreasing rate of parameter ε denotes that the difference in the enhancement of the elastic moduli between the two directions relative to the fractures is smaller than before. This confirms our interpretation in terms of the continuously bridging hydrate in the fractures.

Fig. 5 also shows that with the dissociating hydrate, ε quickly increases first and then its variation tends to be stable. Such variation in ε during hydrate dissociation suggests that the reduction in the elastic moduli perpendicular to the fractures is first more significant than that at the parallel direction, and then the decreasing trend of the two elastic moduli is similar. This enhances our confidence in the proposed explanation that the bridging hydrate slowly evolves to floating hydrate in the fractures during hydrate dissociation.

In addition to showing the distinct variations of the parameter ε with increasing and decreasing hydrate saturation, Fig. 5 also interestingly shows that the value of ε (about 0.11) at the hydrate saturation of about 27% during hydrate dissociation is significantly greater than that (about 0.04) at the same hydrate saturation during hydrate formation. This can be attributed to the different effects of hydrate distribution on the anisotropic elastic properties between hydrate formation and dissociation. As presented in the previous, the highest hydrate saturation in sample F-90 is about 27%, while it is about 30% in sample F-0 (see Fig. 4). Therefore, the parameter ε is only calculated to the hydrate saturation of about 27%. The difference in the highest hydrate saturation between the two samples does not impact ε during hydrate formation but can affect the anisotropic parameter during hydrate dissociation. Because the hydrate is dissociating in the sample F-0 from 30% to 27%, the bridging hydrate has partially transformed to floating hydrate at 27% hydrate saturation, and therefore $V_P(0^\circ)$ at this hydrate saturation during hydrate dissociation is significantly lower than that at the same hydrate saturation during hydrate formation. On the other hand, $V_P(90^\circ)$ at the hydrate saturation of 27% stays the same because there is no hydrate dissociating, and as a result the parameter ε is dramatically higher at this dissociating hydrate saturation compared to that during hydrate formation. It is also because the hydrate in the sample F-0 is dissociating earlier than in the sample F-90, $V_P(0^\circ)$ with decreasing hydrate saturation is more

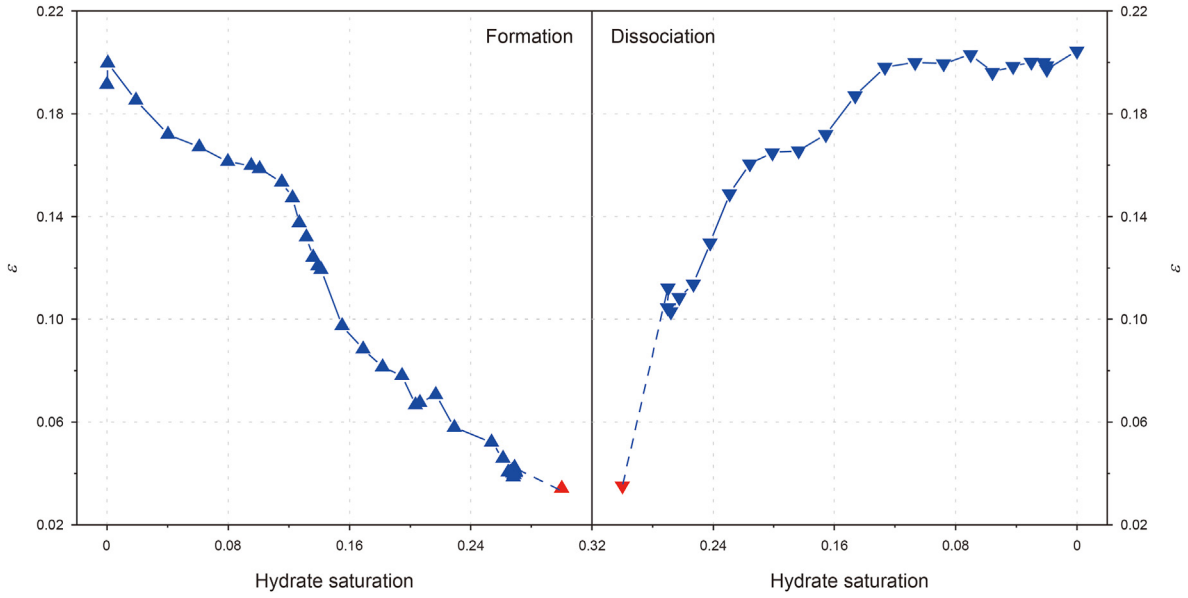

Fig. 5. Changes in the compressional wave anisotropic parameter during hydrate formation and dissociation. Because the highest hydrate saturation in the sample F-90 is about 27%, the parameter ε is only calculated to the hydrate saturation of about 27% although the highest hydrate saturation in the sample F-0 is about 30%. To clearly show that the highest hydrate saturation of the actually calculated parameter ε is about 27% rather than 30%, the expected values of parameter ε at the hydrate saturation of 30% for hydrate formation and dissociation that should be equal according to the reported results by Liu et al. (2021b), are plotted and respectively represented by the red up and down triangles.

significantly slower than its value at the same increasing hydrate saturation in comparison with the difference in $V_P(90°)$. Accordingly, the parameter ε during hydrate dissociation is systematically higher than that for hydrate formation throughout the saturation range, and this is clearly illustrated in Fig. 5. The observed difference in the values of parameter ε at the same hydrate saturation between hydrate formation and dissociation highlights the importance of knowing the hydrate distribution in the accurate assessment of hydrate resources from elastic measurements.

3.2. Effects of hydrate evolution on the anisotropic electrical properties

The experimentally measured anisotropic electrical conductivities of the samples with varying hydrate saturation during hydrate formation and dissociation are plotted in Fig. 6. During hydrate formation, both the electrical conductivities gently increase at the lower hydrate saturation, and generally decrease with the further increasing hydrate saturation. For hydrate dissociation, except for the quick increases in $\sigma(0°)$ with the decreasing hydrate saturation from 30% to 27%, the behaviors of the anisotropic electrical conductivities are similar as hydrate saturation is lower than about 27%, i.e., both the electrical conductivities decrease first, then approximately flatly vary, and finally increase rapidly with dissociating hydrate.

For the process of hydrate formation, the measured electrical conductivities can be jointly affected by the salt expulsion effect, the exothermic reaction, and the forming hydrate content (Jin et al., 2020; Ren et al., 2010). The salt expulsion effect of hydrate can increase the salinity of the pore water, and thus would increase the electrical conductivities. The exothermic reaction of hydrate formation can slightly increase the temperature, so that the electrical conductivities would also be enhanced. The increasing hydrate content with low electrical conductivity, on the contrary, would give rise to the decrease in the electrical conductivities. At the lower hydrate saturation, due to the very small amount of the forming hydrate, the effects of hydrate content on the electrical properties may be less significant than that of the salt expulsion effect and the exothermic reaction, resulting in the gentle increase of the electrical conductivities. With the further formation of hydrate, hydrate content continuously increases, so that the effects of hydrate content on reducing the rock conductivities may prevail over that of the salt expulsion effect and the exothermic reaction on increasing the conductivities, leading to the reduction in the electrical conductivities.

Compared with the influencing factors on the electrical conductivities during hydrate formation, more factors will affect the electrical conductivities during hydrate dissociation, including the increasing temperature of the experimental system, the decreasing hydrate content and reducing salinity of pore water, and the generating gas micro-bubbles (insulation) scattering in the pores associated with hydrate dissociation. On the one hand, the increasing temperature of the experimental system for hydrate dissociation and the decreasing hydrate content would elevate the electrical conductivities. On the other hand, the reducing salinity of pore water and forming gas bubbles will decrease the electrical conductivities (Li et al., 2010). Specially, the scattering gas bubbles (microscopic) generated by hydrate dissociation in the pore system may be the leading factor for the lower electrical conductivities at the hydrate saturation of 0 for hydrate dissociation than that at the same hydrate saturation for hydrate formation, as shown in Fig. 6. The above comprehensive effects may give rise to the measured variations in the electrical conductivities. However, it can be difficult to provide an explicit interpretation for the obtained variations based on the current study.

Apart from the overall variations in the electrical conductivities during hydrate formation and dissociation, Fig. 6 also shows that the significant differences between the anisotropic electrical conductivities. It is clear that the electrical conductivities of sample F-90 (i.e., $\sigma(90°)$) are systematically higher than that of sample F-0 (i.e., $\sigma(0°)$). This is because the aligned fractures in sample F-90 are parallel to the applied electrical field, and hence show greater ability for the movement of electrical charges (Han et al., 2019). In addition to the differences in the values between the anisotropic electrical conductivities, the varying trends of the two electrical conductivities with hydrate saturation are also significantly different, especially during hydrate formation. Fig. 6 shows the gentle increase of the two electrical conductivities at the beginning stage of hydrate formation, and the dramatically steeper decreasing trend of $\sigma(90°)$ than that of $\sigma(0°)$ with the further increasing

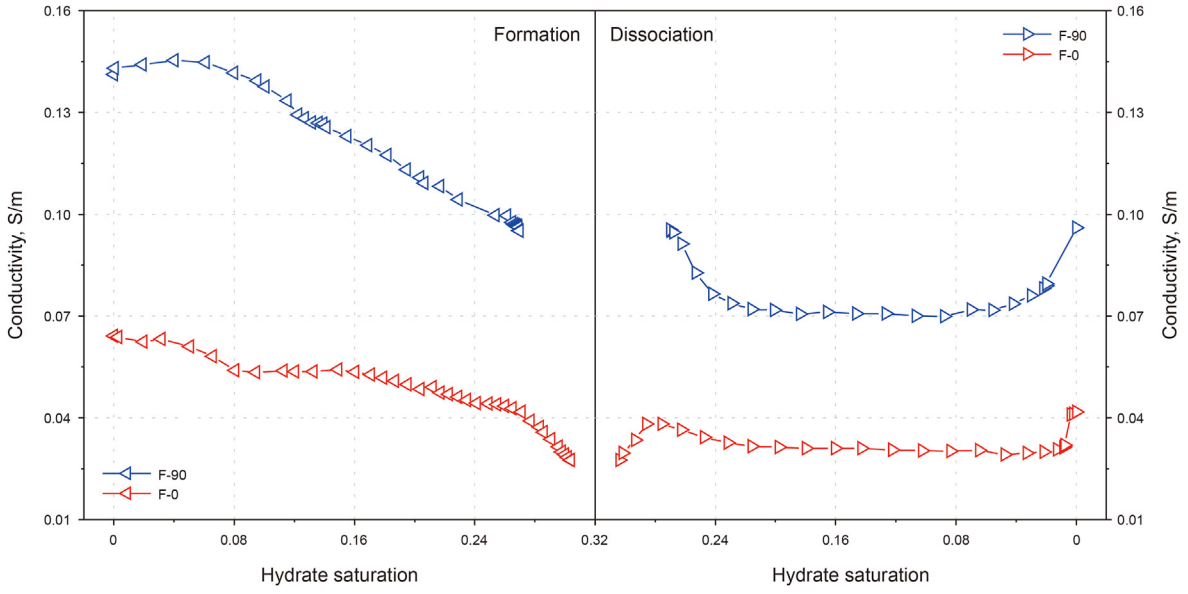

Fig. 6. Variations of the measured anisotropic electrical conductivities as functions of hydrate saturation during hydrate formation and dissociation.

hydrate saturation. According to the understanding of the hydrate distribution in the fractures obtained from the anisotropic elastic properties, the significantly steeper decreasing trend of $\sigma(90^\circ)$ than $\sigma(0^\circ)$ may be explained in terms of the hydrate with bridging distribution between the nearby surfaces of the fractures. The bridging hydrate between the two surfaces is dispersed in the fractures, and thus can be regarded as column-like substance. This dispersed column-like bridging hydrate can narrow a bit the conductive paths in the direction across the fractures, but will significantly increase the tortuosity of the conductive paths along the fractures. Therefore, the conductivity parallel to the fractures is weakened to a greater extent than that perpendicular to the fractures.

Similar to the above anisotropic electrical conductivities, the electrical anisotropic parameter (λ) is another reliable means to directly characterize the electrical anisotropy of the samples with aligned fractures. Fig. 7 shows the variation of the parameter λ with increasing and decreasing hydrate saturation. It can also be seen from Fig. 7 that parameter λ quickly increases at hydrate saturation below about 10%, and then rapidly decreases until hydrate saturation reaches about 16%, after which λ gradually balances. Considering that both the anisotropic electrical conductivities initially increase and then decrease as hydrate further forms, the initial increase in parameter λ indicates that the enhancement in $\sigma(90^\circ)$ is faster than that of $\sigma(0^\circ)$ at the beginning stage of hydrate formation ($S_h < 10$). The subsequent increase in parameter λ with the further increasing hydrate saturation ($10\% < S_h < 16\%$) implies the rapider decreasing rate of $\sigma(0^\circ)$ than $\sigma(90^\circ)$. For the range of hydrate saturation from about 16% to 27%, combining with the decreasing electrical conductivities, the gradual balance of parameter λ suggests that the decreasing rates of $\sigma(0^\circ)$ and $\sigma(90^\circ)$ become consistent by degrees.

Fig. 7 also shows the behavior of parameter λ with dissociating hydrate. With the decreasing hydrate saturation, parameter λ rapidly decreases in the range of hydrate saturation from about 27% to 24%. As hydrate further dissociates, parameter λ slightly increases for the hydrate saturation interval between about 24% and 9%, and the increasing trend becomes significantly steeper when hydrate saturation decreases from about 9% to 2%. For the final stage of hydrate dissociation ($S_h < 2\%$), parameter λ sharply decreases. According to the general decrease in the two electrical conductivities at the range of hydrate saturation from about 27% to 24%, the reduction in parameter λ reflects the rapider decreasing rate of $\sigma(90^\circ)$ than $\sigma(0^\circ)$, which is clearly shown in Fig. 6. As hydrate saturation decreases from about 24% to 9%, the gentle increase of parameter λ denotes the slight difference in the variation between the anisotropic electrical properties, i.e., $\sigma(0^\circ)$ gently decreases, while $\sigma(90^\circ)$ weakly decreases first and then is almost unchanged. The fast enhancement in parameter λ, at the interval of hydrate saturation between about 9% and 2%, can be regarded as the response of the quick increase in $\sigma(90^\circ)$ and the slight decrease in $\sigma(0^\circ)$, as can be seen in Fig. 6. For the final stage of hydrate dissociation ($S_h < 2\%$), taking into account the increase in the two electrical conductivities, the sharp decrease in parameter λ implies that the increase in $\sigma(0^\circ)$ is significantly faster than that of $\sigma(90^\circ)$.

3.3. Effects of hydrate evolution on the anisotropic joint elastic-electrical properties during hydrate formation

We have analyzed and interpreted the behaviors of the anisotropic elastic and electrical properties during hydrate formation and dissociation. In this section, we further explore the relationships between the anisotropic elastic and electrical properties (i.e., the anisotropic joint elastic-electrical properties) during hydrate formation. We focus only on the joint behaviors with forming hydrate, because the anisotropic electrical properties during hydrate dissociation can be difficult to explain since there are so many factors influencing the results as discussed in the previous sections.

Fig. 8 illustrates the correlations between the anisotropic elastic and electrical properties and their dependence on increasing hydrate saturation. It can be seen that apart from the initial increase in $\sigma(90^\circ)$, the electrical conductivities generally decrease with increasing compressional wave velocities as an implicit function of increasing hydrate saturation, i.e., the elastic and electrical properties are negatively correlated with the forming hydrate. Such a general negative correlation can be easily explained by the fact that hydrate simultaneously enhances the elastic velocities and reduces the electrical conductivities, as demonstrated above.

We have demonstrated in the previous sections that the evolution of hydrate distribution during hydrate formation can significantly affect the velocity across the fractures ($V_P(0^\circ)$) but has slight impacts on the velocity along the fractures ($V_P(90^\circ)$). On the other hand for the electrical properties during hydrate formation, although both the conductivities are not dramatically affected by the evolving hydrate, the extent of the overall variation in the

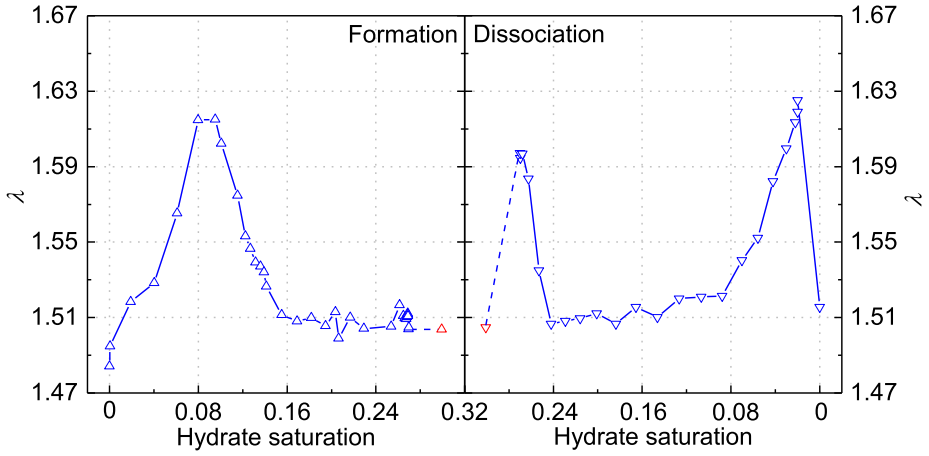

Fig. 7. Changes in the electrical anisotropic parameter during hydrate formation and dissociation. Similar to the highest hydrate saturation of parameter ε, the parameter λ is also calculated to the hydrate saturation of about 27%. To clearly show that the highest hydrate saturation of the actually calculated parameter λ is about 27% rather than 30%, the expected value of parameter λ at the hydrate saturation of 30% for hydrate formation and dissociation that would be equal based on the understanding of parameter ε reported by Liu et al. (2021b), are plotted and respectively represented by the red up and down triangles.

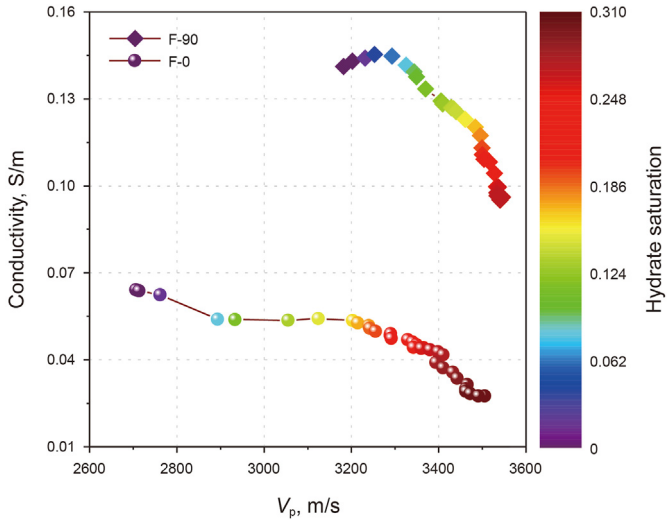

Fig. 8. Behaviors of the anisotropic joint elastic-electrical properties with hydrate saturation during hydrate formation.

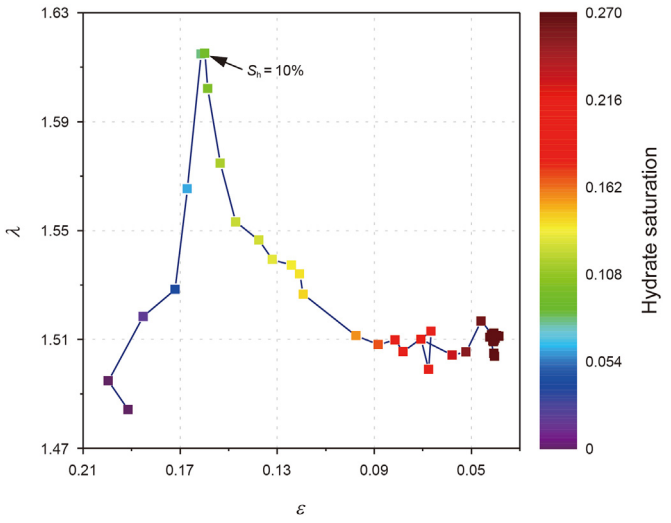

Fig. 9. Dependence of the joint elastic-electrical anisotropic parameters on the increasing hydrate saturation during hydrate formation.

conductivity parallel to the fractures ($\sigma(90°)$) is greater than that at the perpendicular direction ($\sigma(0°)$). In view of the significant variation in $V_P(0°)$ and $\sigma(90°)$ with the evolving hydrate, the two properties may be used to accurately estimate hydrate saturation. However, there is a condition that the hydrate distribution must be clearly understood in advance due to their dramatic effects on the two properties. By contrast, given the less notable variation in $V_P(90°)$ and $\sigma(0°)$, the two properties can be used to evaluate hydrate saturation without the knowledge of hydrate distribution, but the results may be less accurate because the overall dependence of $V_P(90°)$ and $\sigma(0°)$ on hydrate saturation is less notable.

Although the evolving hydrate during hydrate formation is significantly affecting the varying trends of $V_P(0°)$ and $\sigma(90°)$, the joint elastic-electrical properties of the samples in both the two directions are relatively smooth, besides the slight increase at the lower hydrate saturation in the sample F-90, as shown in Fig. 8. This may be due to the fact that the less dramatic impact of hydrate distribution on $\sigma(0°)$ and $V_P(90°)$ is neutralizing partially the significant variation of $V_P(0°)$ and $\sigma(90°)$, respectively, making the joint correlations less dependent on the hydrate distribution. In addition to the smooth variation of both the joint correlations, Fig. 8 also shows that the slope of the sample F-90 is much steeper than that of the sample F-0. These characteristics imply that the joint properties in both directions can be employed for the quantification of hydrate without the knowledge of hydrate distribution and the assessment using the physical properties parallel to the fractures will give better results, implicating the more valuable of the collected survey data parallel to the fractures than that at the perpendicular direction for the accurate estimation of hydrate resources in the fractured reservoirs. This is the main advantage of the joint properties over the single elastic or electrical property for the estimation of hydrate amount.

However, since the joint properties in Fig. 8 contain less information about the hydrate distribution, which can be important for the strategy design for the development of natural gas in hydrate reservoirs, it is seemingly that the single physical property is better than the joint properties for the discrimination of hydrate distribution during the development of gas in hydrate reservoirs. Nevertheless, the joint correlation between the elastic and electrical anisotropic parameters demonstrated in Fig. 9 shows a sharp peak at the hydrate saturation of about 10%, which is the saturation point that the hydrate starts to bridge in the fractures, and therefore can clearly discriminate the main pattern of hydrate distribution in the fractures. This compensates for the weakness of the joint correlations in Fig. 8 for the identification of hydrate distribution, and illustrates that the combination of the joint elastic-electrical correlations and the joint anisotropic parameters (i.e., the anisotropic joint elastic-electrical properties) can be employed not only to accurately estimate hydrate saturation during hydrate exploration but also to identify hydrate distribution in the fractures for the development of hydrate.

4. Discussion

We have studied the anisotropic elastic and electrical properties in the synthetic fractured sandstones with forming and dissociating hydrate. During hydrate formation and dissociation, in addition to the impact of the hydrate itself (including hydrate saturation and distribution), the varying pore pressure associating with the hydrate can affect the elastic properties, and both the varying pore pressure and temperature can influence the electrical properties. Liu et al. (2021b) have performed the comparative experiments based on a synthetic rock with aligned fractures to understand the effects of hydrate and the varying pore pressure on the elastic properties. It is found that compared with the contribution of hydrate, the effects of the variation in pore pressure on the elastic properties can be negligible, and therefore the behaviors of the anisotropic elastic velocities of the fractured samples during hydrate formation and dissociation were mainly attributed to the hydrate (Liu et al., 2021b). Considering the effects of the varying pore pressure on the anisotropic elastic properties are already clear, we focus in this work only on distinguishing the effects of hydrate and the varying pore pressure and temperature on the electrical properties.

The monitored variation of the anisotropic electrical conductivities with pore pressure regulated by nitrogen is shown in Fig. 10a. It can be seen that both the conductivities slightly increase with reducing pore pressure. This is opposite to the experimental results based on brine saturated isotropic rocks reported by Han et al. (2021a), who found that the decreasing pore pressure will reduce the conductivity because of the closure of the micropores and compliant pores (low-aspect-ratio pores) that will reduce to connectivity of the stiff pores full of brine. The obtained increasing electrical conductivities with decreasing pore pressure are possibly

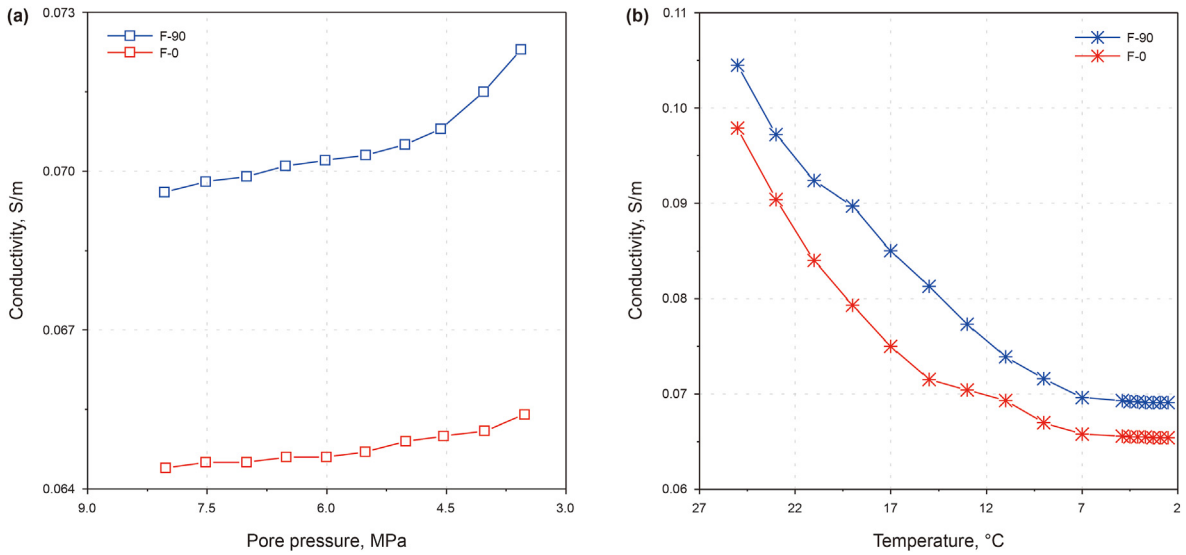

Fig. 10. Changes in the anisotropic electrical conductivities with varying (a) pore pressure and (b) temperature. Note that the pore pressure and temperature variations presented in the horizontal ordinate are in descending order, to be consistent with the varying order of the pore pressure and temperature during hydrate formation.

due to the fact that our samples are filled with both brine and insulating gas (i.e., partially saturated) and the compression of the micropores and compliant pores may expel more brine into the stiff pores, making the rock more conductive because the stiff pores containing more brine can provide the more conductive pathway than the micropores and compliant pores. Comparing with the overall reduction in the conductivities with the forming hydrate (when the pore pressure also reduces) as shown Fig. 6, it is evident that reduction in the conductivities caused by the hydrate is playing a dominant role over the changing pore pressure.

Fig. 10b shows the collected variation of the anisotropic conductivities with temperature reducing from 25 °C to 2.5 °C to cover the range of temperature variation of the experimental system during hydrate formation and dissociation. As expected, both the conductivities reduce gradually with decreasing temperature, and the reduction becomes diminishing from 5 °C to 2.5 °C that is a greater temperature range than observed for the hydrate formation, which is approximately from 3 °C to 2.5 °C. The almost unchanging electrical conductivities from 3 °C to 2.5 °C indicates that temperature is not playing a significant role on the electrical properties during hydrate formation where the forming hydrate is the main reason for the reducing anisotropic conductivities. Since the conductivities notably vary with the temperature between 2.5 °C and 24 °C, as shown Fig. 10b, the conductivities with dissociating hydrate can be significantly affected by the varying temperature due to the broad range of the temperature variation and the greater impacts of temperature on the conductivities at the higher temperature range. This also explains why we did not explain the electrical properties with dissociating hydrate in detail and why we did not show the joint elastic-electrical properties during hydrate dissociation, in the previous sections.

The above results of the comparative experiments confirm that the existence of hydrate and its distribution are the main contribution to the observed variation of anisotropic elastic and electrical properties, which implicitly imply that the observed behaviors of the anisotropic elastic and electrical properties can be interpreted in terms of the varying hydrate saturation and distribution in the fractures as offered in this study, except for the variation in the conductivities during hydrate dissociation. However, the provided interpretation still needs to be verified by appropriate theoretical models. For the fractured hydrate-bearing reservoirs, although several anisotropic models have been developed to investigate the anisotropic elastic and electrical properties (Ghosh et al., 2010; Lee and Collett, 2009, 2012), they generally ignore the effects of the hydrate distribution in the fractures on the anisotropic properties, making the models unable to predict the physical properties with varying hydrate distribution. Therefore, the theoretical modeling of the anisotropic elastic, electrical and joint elastic-electrical properties in the fractured hydrate-bearing reservoirs remains challenging but will form the topic for our future studies.

The reasonable interpretations of the measured anisotropic elastic and electrical properties during hydrate formation suggest that the evolution of hydrate distribution from binding to bridging in the fractures starts at the hydrate saturation of about 10%. The sharp peak of the joint elastic-electrical anisotropic parameters at the hydrate saturation of about 10%, as shown in Fig. 9, could be regarded as a more apparent phenomenon indicating the evolution of hydrate distribution. The hydrate saturation point ($S_h = 10\%$) is the effective hydration saturation in the normal pores and fractures of samples. Therefore, this 10% hydrate saturation point might change for the samples with various fracture thicknesses and porosities. On the one hand, when the porosity of the samples is equal to that of our samples, the hydrate saturation point would respectively reduce and increase with the decreasing and increasing fracture thickness (i.e., the change in the distance between the nearby surfaces of factures), because the hydrate can easier and more difficult (the required amount of hydrate in the fractures respectively decrease and increase) to bridge the nearby surfaces of the factures, respectively. On the other hand, for the samples with the same fracture thickness as our samples, the amount of hydrate in the fractures that is required to bridge the surfaces of the fractures could be not affected, so that the effective hydrate saturation point would increase and decrease when their porosity is lower and bigger than that of our samples, respectively. Although the 10% hydrate saturation point suggested this study would change with the various samples, the observed behaviors of the anisotropic properties that could be employed to understand the evolution of hydrate distribution in the fractures, would be similar.

We employ two samples with aligned fractures (i.e., sample F-0 and F-90, as shown in Fig. 2) to measure the anisotropic compressional wave velocities and electrical conductivities during

hydrate formation and dissociation. This is because the experimental device can only synchronously measure the elastic and electrical properties at the normal direction of the end of the samples. The synchronous measurement of the anisotropic elastic and electric properties in a single sample with aligned fractures that is similar to the method for obtaining the anisotropic elastic properties reported by Liu et al. (2021b), is the best experimental method to study the anisotropic joint elastic-electric properties. However, the experimental device for synchronously measuring the anisotropic elastic and electric properties in a single sample is not developed yet. The comparison of the anisotropic elastic properties between the presented in this study and the reported by Liu et al. (2021b) based on a single sample shows that the overall behaviors of the anisotropic velocities and parameter ε with forming and dissociating hydrate are similar, while the value of parameter ε at the highest hydrate saturation between hydrate formation and dissociation is equal in the obtained results by Liu et al. (2021b), but is different in this study (as shown in Fig. 5). This is because the highest hydrate saturation influencing the elastic properties at the directions perpendicular and parallel to the fractures in a single sample is equal, so that the evolution of hydrate distribution in the single sample could synchronously affect the anisotropic elastic properties, leading to the equal parameter ε at the highest hydrate saturation between formation and dissociation. Nevertheless, the difference in the highest hydrate saturation in two samples gives rise to the distinct effects of the hydrate distribution evolution on the anisotropic elastic properties during hydrate dissociation, which have been detailed explained in the previous paragraph. However, the similar behaviors in the anisotropic velocities and parameter ε with evolving hydrate between the two experimental methods and the reasonable analysis and explanations of the experimental results presented this study illustrate that the experimental method in this study can be employed to investigate the responses of the anisotropic elastic, electrical, and joint elastic-electrical properties on the evolving hydrate in the samples with aligned fractures.

5. Conclusions

We have designed and implemented dedicated laboratory experiments to investigate the anisotropic elastic, electrical, and joint elastic-electrical properties in the fractured artificial samples with evolving hydrate. The following knowledge can be obtained from the results and analyses presented in this study:

1) The velocity perpendicular to the fractures increased with more significantly varying trend during hydrate formation and decreased with greater extent for dissociation than that parallel to the fractures, respectively. The electrical conductivity parallel to the fractures more steeply decreased than that perpendicular to the fractures during hydrate formation, besides the slight increase in the conductivities at the beginning stage of hydrate formation. In the process of hydrate dissociation, except for the increase of the conductivity across the fractures at the beginning stage, the conductivities decreased first, then gently varied, and finally increased. The elastic and electrical anisotropic parameters significantly varied with forming and dissociating hydrate.
2) The experimental results were plausibly explained and interpreted in terms of the evolution of hydrate distribution in the fractures. The binding hydrate (hydrate binds to the grains) evolved to bridge the surfaces of the fractures as hydrate saturation exceeded about 10% during hydrate formation. For hydrate dissociation, the bridging hydrate slowly transformed to floating hydrate in the fractures.
3) The correlations between the anisotropic velocities and conductivities varied with approximately consistent trends of different slopes, and there was a sharp peak of the joint anisotropic parameters at the hydrate saturation of about 10%. The joint elastic-electrical properties were found to be suitable for the accurate estimation of hydrate saturation during hydrate exploration and for the identification of hydrate distribution in the fractures for the development of natural gas in hydrate reservoirs.

Acknowledgments

We would like to acknowledge the financial supports received from the National Natural Science Foundation of China (42174136, 41821002 and 41874151), and the Shandong Provincial Natural Science Foundation, China (ZR2021JQ14).

References

Archer, D., Buffett, B., Brovkin, V., 2009. Ocean methane hydrates as a slow tipping point in the global carbon cycle. Proc. Natl. Acad. Sci. U. S. A. 106, 20596–20601. https://doi.org/10.1073/pnas.0800885105.

Attias, E., Amalokwu, K., Watts, M., Falcon-Suarez, I.H., North, L., Hu, G.W., Best, A.I., Weitemeyer, K., Minshull, T.A., 2020. Gas hydrate quantification at a pockmark offshore Norway from joint effective medium modelling of resistivity and seismic velocity. Mar. Petrol. Geol. 113, 104151. https://doi.org/10.1016/j.marpetgeo.2019.104151.

Attias, E., Weitemeyer, K., Minshull, T.A., Best, A.I., Sinha, M., Jegen-Kulcsar, M., Holz, S., Berndt, C., 2016. Controlled-source electromagnetic and seismic delineation of subseafloor fluid flow structures in a gas hydrate province, offshore Norway. Geophys. J. Int. 206, 1093–1110. https://doi.org/10.1093/gji/ggw188.

Boswell, R., Collett, T.S., 2011. Current perspectives on gas hydrate resources. Energy Environ. Sci. 4, 1206–1215. https://doi.org/10.1039/c0ee00203h.

Bu, Q.T., Hu, G.W., Liu, C.L., X, T.J., Li, C.F., Meng, Q.G., 2019. Acoustic characteristics and micro-distribution prediction during hydrate dissociation in sediments from the south China sea. J. Nat. Gas Sci. Eng. 65, 135–144. https://doi.org/10.1016/j.jngse.2019.02.010.

Cook, A.E., 2010. Gas Hydrate-Filled Fracture Reservoirs on Continental Margins. Dissertation for Doctoral Degree. Columbia University, New York.

Cortes, D.D., Martin, A.I., Yun, T.S., Francisca, F.M., Santamarina, J.C., Ruppel, C., 2009. Thermal conductivity of hydrate-bearing sediments. J. Geophys. Res. Solid Earth 114, B11103. https://doi.org/10.1029/2008JB006235.

Dai, S., Santamarina, J.C., Waite, W.F., Kneafsey, T.J., 2012. Hydrate morphology: physical properties of sands with patchy hydrate saturation. J. Geophys. Res. Solid Earth 117, B11205. https://doi.org/10.1029/2012JB009667.

Daigle, H., Dugan, B., 2010. Origin and evolution of fracture-hosted methane hydrate deposits. J. Geophys. Res. Solid Earth 115, B11103. https://doi.org/10.1029/2010JB007492.

Ding, P.B., Di, B.R., Wang, D., Wei, J.X., Li, X.Y., 2017. Measurements of seismic anisotropy in synthetic rocks with controlled crack geometry and different crack densities. Pure Appl. Geophys. 174, 1907–1922. https://doi.org/10.1007/s00024-017-1520-3.

Ghosh, R., Sain, K., Ojha, M., 2010. Effective medium modeling of gas hydrate-filled fractures using the sonic log in the Krishna-Godavari basin, offshore eastern India. J. Geophys. Res. Solid Earth 115, B06101. https://doi.org/10.1029/2009JB006711.

Goswami, B.K., Weitemeyer, K.A., Minshull, T.A., Sinha, M.C., Westbrook, G.K., Chabert, A., Henstock, T.J., Ker, S., 2015. A joint electromagnetic and seismic study of an active pockmark within the hydrate stability field at the Vestnesa Ridge, West Svalbard margin. J. Geophys. Res. Solid Earth 120, 6797–6822. https://doi.org/10.1002/2015JB012344.

Han, T.C., 2018. Joint elastic-electrical properties of artificial porous sandstone with aligned fractures. Geophys. Res. Lett. 45, 3051–3058. https://doi.org/10.1002/2018GL077541.

Han, T.C., Best, A.I., MacGregor, L.M., Sothcott, J., Minshull, T.A., 2011. Joint elastic-electrical effective medium models of reservoir sandstones. Geophys. Prospect. 59, 777–786. https://doi.org/10.1111/j.1365-2478.2011.00956.x.

Han, T.C., Josh, M., Liu, H., 2019. Effects of aligned fractures on the dielectric properties of synthetic porous sandstones. J. Pet. Sci. Eng. 172, 436–442. https://doi.org/10.1016/j.petrol.2018.09.093.

Han, T.C., Liu, S.B., Fu, L.Y., Yan, H., 2021a. Understanding how overpressure affects the physical properties of sandstones. Geophysics 86, MR203–MR210. https://doi.org/10.1190/geo2020-0776.1.

Han, T.C., Liu, S.B., Xu, D.H., Fu, L.Y., 2020. Pressure-dependent cross-property relationships between elastic and electrical properties of partially saturated porous sandstones. Geophysics 85, MR107–MR115. https://doi.org/10.1190/geo2019-0477.1.

Han, T.C., Yan, H., Li, B., Fu, L.-Y., 2021b. Pressure-dependent joint elastic–electrical

properties in brine-saturated artificial sandstones with aligned penny-shaped cracks—Part I: experimental results. Geophys. J. Int. 228, 1071–1082. https://doi.org/10.1093/gji/ggab386.
Hu, G.W., Ye, Y.G., Zhang, J., Diao, S.B., Liu, C.L., 2012. Acoustic properties of hydrate-bearing unconsolidated sediments measured by the bender element technique. Chin. J. Geophys. 55 (6), 635–647. https://doi.org/10.1002/cjg2.1758.
Hu, G.W., Ye, Y.G., Zhang, J., Liu, C.L., Diao, S.B., Wang, J.S., 2010. Acoustic properties of gas hydrate-bearing consolidated sediments and experimental testing of elastic velocity models. J. Geophys. Res. 115, B02102. https://doi.org/10.1029/2008JB006160.
Jin, Y.R., Li, S.X., Yang, D., 2020. Experimental and theoretical quantification of the relationship between electrical resistivity and hydrate saturation in porous media. Fuel 269, 117378. https://doi.org/10.1016/j.fuel.2020.117378.
Kumar, D., Sen, M.K., Bangs, N.L., Wang, C., Pecher, I., 2006. Seismic anisotropy at hydrate ridge. Geophys. Res. Lett. 33, L01306. https://doi.org/10.1029/2005GL023945.
Kvenvolden, K.A., 1993. Gas hydrates—geological perspective and global change. Rev. Geophys. 31, 173–187. https://doi.org/10.1029/93RG00268.
Lee, M.W., 2009. Anisotropic Velocities of Gas Hydrate-Bearing Sediments in Fractured Reservoirs. USGS Scientific Investigation Report. https://doi.org/10.3133/sir20095141.
Lee, M.W., Collett, T.S., 2012. Pore- and fracture-filling gas hydrate reservoirs in the gulf of Mexico gas hydrate joint industry project leg II green canyon 955 H well. Mar. Petrol. Geol. 34, 62–71. https://doi.org/10.1016/j.marpetgeo.2011.08.002.
Lee, M.W., Collett, T.S., 2009. Gas hydrate saturations estimated from fractured reservoir at Site NGHP-01-10, Krishna-Godavari Basin, India. J. Geophys. Res. Solid Earth 114, B07102. https://doi.org/10.1029/2008JB006237.
Li, S.X., Xia, X.R., Xuan, J., Liu, Y., Li, Q., 2010. Resistivity in formation and decomposition of natural gas hydrate in porous medium. Chin. J. Chem. Eng. 18, 39–42. https://doi.org/10.1016/S1004-9541(08)60320-1.
Li, Y.L., Sun, H.L., Meng, Q.G., Liu, C.L., Chen, Q., Xing, L.C., 2020. 2-D electrical resistivity tomography assessment of hydrate formation in sandy sediments. NGI. B. 7, 278–284. https://doi.org/10.3787/j.issn.1000-0976.2019.10.017.
Liu, S.B., Han, T.C., Fu, L.Y., 2021a. Distribution of gas hydrate in fractured reservoirs: insights from anisotropic seismic measurements. Sci. China Earth Sci. 64, 744–752. https://doi.org/10.1007/s11430-020-9725-0.
Liu, S.B., Han, T.C., Fu, L.Y., 2021b. Laboratory investigations of acoustic anisotropy in artificial porous rock with aligned fractures during gas hydrate formation and dissociation. J. Geophys. Res. Solid Earth 126, e2021JB021678. https://doi.org/10.1029/2021JB021678.
Liu, T., Liu, X.W., Zhu, T., 2020. Joint analysis of P-wave velocity and resistivity for morphology identification and quantification of gas hydrate. Mar. Petrol. Geol. 112, 104036. https://doi.org/10.1016/j.marpetgeo.2019.104036.
Liu, Y.Z., Zhang, L.X., Yang, L., Dong, H.S., Zhao, J.F., Song, Y.C., 2021. Behaviors of co2 hydrate formation in the presence of acid-dissolvable organic matters. Environ. Sci. Technol. 55, 6206–6213. https://doi.org/10.1021/acs.est.0c06407.
Mavko, G., Mukerji, T., Dvorkin, J., 2009. The Rock Physics Handbook, second ed. Cambridge University, New York.
Miyakawa, A., Saito, S., Yamada, Y., Tomaru, H., Kinoshita, M., Tsuji, T., 2014. Gas hydrate saturation at site c0002, IODP expeditions 314 and 315, in the kumano basin, nankai trough. Isl. Arc 23, 142–156. https://doi.org/10.1111/iar.12064.
Nabawy, B.S., Rochette, P., Geraud, Y., 2010. Electric pore fabric of the Nubia sandstones in south Egypt: characterization and modelling. Geophys. J. Int. 183, 681–694. https://doi.org/10.1111/j.1365-246X.2010.04789.x.
Peng, C., Zou, C.C., Lu, Z.Q., Yu, C.Q., Liu, A.Q., Tang, Y.Y., Hu, X.D., Zhang, S.X., Wen, H.J., Li, Y.H., Wang, W.C., 2019. Evidence of pore- and fracture-filling gas hydrates from geophysical logs in consolidated rocks of the muli area, qinghai–Tibetan plateau permafrost, China. J. Geophys. Res. Solid Earth 124, 6297–6314. https://doi.org/10.1029/2018JB016041.
Priest, J.A., Rees, E.V.L., Clayton, C.R.I., 2009. Influence of gas hydrate morphology on the seismic velocities of sands. J. Geophys. Res. Solid Earth 114, B11205. https://doi.org/10.1029/2009JB006284.
Ren, S.R., Liu, Y.J., Liu, Y.X., Zhang, W., 2010. Acoustic velocity and electrical resistance of hydrate bearing sediments. J. Pet. Sci. Eng. 70, 52–56. https://doi.org/10.1016/j.petrol.2009.09.001.
Sahoo, S.K., Madhusudhan, B.N., Marín-Moreno, H., North, L.J., Ahmed, S., Falcon-Suarez, I.H., Minshull, T.A., Best, A.I., 2018a. Laboratory insights into the effect of sediment-hosted methane hydrate morphology on elastic wave velocity from time-lapse 4-D synchrotron X-ray computed tomography. G-cubed 19, 4502–4521. https://doi.org/10.1029/2018GC007710.
Sahoo, S.K., Marín-Moreno, H., North, L.J., Falcon-Suarez, I., Madhusudhan, B.N., Best, A.I., Minshull, T.A., 2018b. Presence and consequences of coexisting methane gas with hydrate under two phase water-hydrate stability conditions. J. Geophys. Res. Solid Earth 123, 3377–3390. https://doi.org/10.1029/2018JB015598.
Sava, D., Hardage, B., Murray, P., DeAngelo, M., 2008. Rock-physics joint inversion of resistivity-log and seismic velocity for hydrate characterization. In: SEG Technical Program Expanded Abstracts. Society of Exploration Geophysicists. https://doi.org/10.1190/1.3059240.
Schindler, M., Batzle, M.L., Prasad, M., 2017. Micro X-Ray computed tomography imaging and ultrasonic velocity measurements in tetrahydrofuran-hydrate-bearing sediments. Geophys. Prospect. 65, 1025–1036. https://doi.org/10.1111/1365-2478.12449.
Singhroha, S., Bünz, S., Plaza-Faverola, A., Chand, S., 2020. Detection of gas hydrates in faults using azimuthal seismic velocity analysis, vestnesa ridge, W-svalbard margin. J. Geophys. Res. Solid Earth 125, e2019JB017949. https://doi.org/10.1029/2019JB017949.
Sloan, E.D., Koh, C.A., 2007. Clathrate Hydrates of Natural Gases, third ed. CRC Press, New York. https://doi.org/10.1201/9781420008494.
Spangenberg, E., Kulenkampff, J., 2006. Influence of methane hydrate content on electrical sediment properties. Geophys. Res. Lett. 33, L24315. https://doi.org/10.1029/2006GL028188.
Sultan, N., Cochonat, P., Foucher, J.P., Mienert, J., 2004. Effect of gas hydrates melting on seafloor slope instability. Mar. Geol. 213, 379–401. https://doi.org/10.1016/j.margeo.2004.10.015.
Thomsen, L., 1986. Weak elastic anisotropy. Geophysics 51, 1954–1966. https://doi.org/10.1190/1.1442051.
Wang, T., Tang, X.M., 2005. Multipole acoustic responses of a prestressed formation: an effective medium approach. Geophysics 70, 35–44. https://doi.org/10.1190/1.1897031.
Xu, S., Tang, X.M., Torres-Verdín, C., Su, Y., 2018. Seismic shear wave anisotropy in cracked rocks and an application to hydraulic fracturing. Geophys. Res. Lett. 45, 5390–5397. https://doi.org/10.1029/2018GL077931.
Yang, L., Falenty, A., Chaouachi, M., Haberthür, D., Kuhs, W.F., 2016. Synchrotron X-ray computed microtomography study on gas hydrate decomposition in a sedimentary matrix. G-cubed 17, 3717–3732. https://doi.org/10.1002/2016GC006521.
You, K., Flemings, P.B., Malinverno, A., Collett, T.S., Darnell, K., 2019. Mechanisms of methane hydrate formation in. Geological Systems. Rev. Geophys. 57, 1146–1196. https://doi.org/10.1029/2018RG000638.
Zhao, J.F., Yang, L., Liu, Y., Song, Y.C., 2015. Microstructural characteristics of natural gas hydrates hosted in various sand sediments. Phys. Chem. Chem. Phys. 17 (35), 22632–22641. https://doi.org/10.1039/c5cp03698d.